Original article

Experimental study on the influence of pore structure on spontaneous imbibition in marine black shale

Changqing Fu[1], Xiang Xu[1], Yi Du[2,3]*, Xin Kou[1]

[1]*College of Geology and Environment, Xi'an University of Science & Technology, Xi'an 710054, P. R. China*

[2]*National and Local Joint Engineering Research Center for Carbon Capture Utilization and Sequestration & State Key Laboratory of Continental Dynamics, Department of Geology, Northwest University, Xi'an 710069, P. R. China*

[3]*Shaanxi Key Laboratory for Carbon Neutral Technology, Northwest University, Xi'an 710069, P. R. China*

Abstract:
Recently, significant progress has been made in the exploration of marine shale gas in the Qiongzhusi Formation of the Sichuan Basin, China. Micro/nanopores within this formation play a crucial role in spontaneous imbibition and subsequent shale gas production. In this paper, to investigate the influence of pore structure in the Qiongzhusi shale on the spontaneous imbibition characteristics, two sets of samples with varying mineral contents were subjected to horizontal and vertical spontaneous imbibition experiments. One-dimensional transverse relaxation time, two-dimensional longitudinal-transverse relaxation time, and layer division transverse relaxation time spectra from low-field nuclear magnetic resonance were analyzed to elucidate fluid migration during spontaneous imbibition as well as contributions from different pore sizes toward the overall imbibition capacity. The results indicated that, among different pore sizes, mesopores have the greatest impact on the imbibition rate of marine carbonaceous shale, followed by micropores and macropores. The organic matter and clay minerals in carbonaceous shale were found to play a significant role in enhancing the permeability and absorption rate by the presence of abundant mesopores. Besides, the bedding development of marine carbonaceous shale in the Qiongzhusi Formation influences the imbibition process. The horizontal samples exhibited lower levels of imbibition efficiency than their vertical counterparts.

1. Introduction

In recent years, shale gas has gained significant research interest as an unconventional natural gas resource due to its abundant reserves and substantial development potential (Zou et al., 2015, 2019). The shale reservoirs of the Qiongzhusi Formation, located in southern Sichuan, China, possess various advantages, such as high organic matter content, moderate burial depth, considerable thickness, substantial hydrocarbon generation potential, and high gas resource (shale gas content ranging from 0.27 to 6.02 m³/t, with an average of 1.90 m³/t), making them highly prospective for resource development. Shale gas exploitation requires the use of hydraulic fracturing technology due to the persistent low porosity and permeability (Barati and Liang, 2014; Middleton et al., 2015; Ma et al., 2023). Once the residual pressure has been relieved, water can enter the pores through spontaneous imbibition under the action of capillary forces (Engelder, 2012; Flewelling and Sharma, 2014). When the direction of imbibition is consistent with that of shale gas production, capillary force becomes the driving force of shale gas migration; otherwise, it creates resistance causing the retention of fracturing fluid, known as the water blocking effect, which can negatively impact shale gas production (Holditch, 1978; Lu et al., 2022). Therefore, water imbibition in shale is considered as a key factor affecting shale gas recovery, and understanding the transport mechanism
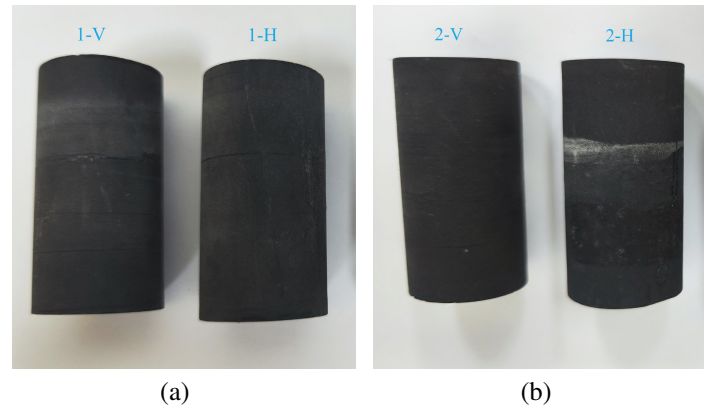
Fig. 1. Shale samples of this study: (a)sample 1 and (b)sample 2.

of the water imbibition process in shale is of great importance for shale gas production (Roychaudhuri et al., 2013; Zhao et al., 2017; Meng et al., 2020; Li et al., 2022a).

Spontaneous imbibition, also known as capillary filling, occurs naturally without external pressure differences (Cai et al., 2014; Dou et al., 2021). The characteristics of shale play a significant role in influencing this process (Yildiz and Akin, 2016; Shen et al., 2017; Cai et al., 2020). Various techniques are available for studying spontaneous imbibition processes, including X-ray scanning, computed tomography, neutron imaging, low field nuclear magnetic resonance (NMR), and numerical simulations (Yue et al., 2019; Lu et al., 2022). NMR is particularly suitable for analyzing the water content during spontaneous imbibition processes in shale samples by examining the relaxation properties of fluid present in pores (Yao et al., 2020). This analytical technique can also assess the contribution of different pore scales to spontaneous imbibition capacity and study the fluid transport mechanisms.

To date, numerous scholars have examined the spontaneous imbibition of shale and its dependence on various factors (Cai and Yu, 2012; Cai, 2021), such as initial water saturation, wettability, mineral composition, bedding, total organic matter (TOC), and liquid properties. Gao et al. (2016) found that the initial water saturation condition affects the shale sample imbibition capacity, which varies with the mineral composition. Xue et al. (2022) discovered that shale imbibition is greatly influenced by directionality. Excessive clay mineral content in shale leads to swelling and pore plugging after imbibition, hindering further imbibition. Gao et al. (2019) observed an increase in imbibition capacity with higher illite clay mineral content in shale samples. Wang et al. (2021) established that the vertical bedding direction limits imbibition, positively correlating it with calcite content but not quartz and clay minerals. Chao et al. (2021) claimed that higher TOC content weakens the imbibition rate of the deep Longmaxi Formation shale, while inorganic salt solutions, especially potassium chloride solution, inhibit shale imbibition and the inhibition strength increases with salinity. Based on an NMR-based study of the imbibition process, Zhu et al. (2023) concluded that micropores have the largest cumulative proportion of water absorption, followed by mesopores, and macropores make up

the lowest cumulative proportion. Zhu et al. (2022) conducted NMR tests to study the distribution dynamics of water during imbibition, and found that micropores and microfractures are filled earlier than macropores and macrofractures for shale samples. The aforementioned studies have investigated numerous factors influencing the spontaneous imbibition of shale; however, most of the research on pore structure has been based on alternative methods, with limited utilization of the NMR method. This paper employs the NMR method to examine the characteristics and impact of pore structure at each stage of the shale spontaneous imbibition process, which holds significant importance for comprehending the mechanism behind shale spontaneous imbibition and fluid distribution.

We utilized NMR technology to investigate the pore structure characteristics and spontaneous imbibition process of marine shale in the Qiongzhusi Formation. The total transverse relaxation time (T_2) spectrum, longitudinal-transverse relaxation time (T_1-T_2) spectrum, and layer division T_2 spectrum of saturated samples, centrifuged samples and samples during the spontaneous imbibition process were tested. Then, the impact of different pore sizes on the imbibition rate of shale reservoirs was assessed, along with the disparities in the spontaneous imbibition process between horizontally and vertically laminated samples. Furthermore, an in-depth analysis was conducted to identify factors contributing to variations in shale sample imbibition efficiency.

2. Methodology

2.1 Samples

The experimental shale samples were collected from the Qiongzhusi Formation in Southern Sichuan. The samples were immediately sealed in a rigid foam box and transported to the laboratory for analysis. The basic rock characteristic analysis of the samples was then carried out, including total TOC, X-ray diffraction analysis and vitrinite reflectance measurements (R_o). The results are summarized in Table 1.

The shale samples were obtained by drilling cylindrical cores (26 mm diameter, 50.5 mm length) along both horizontal and vertical layers (Fig. 1). These samples included 1-V and 2-V, representing the vertical layer drilling samples, and 1-H

Table 1. Basic information of the shale samples.

| Sample | Mineral component content (%) | | | | | | Crystallinity (%) | TOC (%) | R_o (%) | |
	Quartz	Albite	Illite	Kaolinite	Pyrite	Dolomite			Min	Max
1-V, 1-H	27.4	26.1	26.3	1.4	5.1	13.7	73.71	3.65	1.70	2.00
2-V, 2-H	21.0	27.2	43.0	2.8	6.0	0	61.92	3.63	1.63	1.83
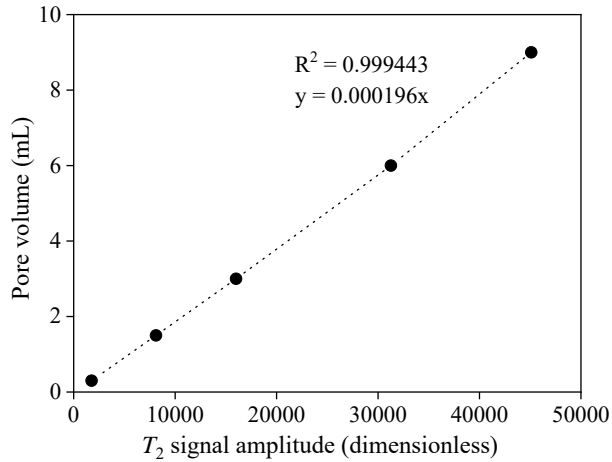
Fig. 2. Linear relationship between the calibrated cumulative signal amplitude and the pore volume.

and 2-H, signifying the horizontal layer drilling samples.

2.2 Experimental instrumentation and parameters

The low-field NMR core analysis system used in this study was the MacroMR12-150HTHP-I model manufactured by Suzhou Niumag Nuclear Magnetic Analysis Instrument Co., Ltd. (Suzhou, China) The magnetic field strength of the permanent magnet is 0.3 ± 0.05 T. To maintain a constant magnet temperature, a nonlinear temperature controller was employed, with the temperature set at 25 °C. To measure the distribution of fluids in pores of various sizes within porous media, the commonly utilized sequence is the hard pulse CARR Purcell Meiboom Gill . T_1-T_2 maps were measured by the Inversion Recovery-Carr-Purcell-Meiboom-Gill sequence. The specific test parameters were as follows: the echo time was set to 0.1 ms, the number of echoes was 10,000, the waiting time was 2,000 ms, and the number of scans was 16.

2.3 Experimental procedure

The instrument was calibrated prior to the experiments to minimize the systematic errors. Calibration involved establishing a correlation between the T_2 relaxation spectrum peak area of water in shale and the water volume. Standard samples with pore volumes of 0.3, 1.5, 3, 6, and 9 mL were utilized, and the volume of each standard sample was 30 mL. The inversion analysis of measured data using rock core analysis software revealed a significant linear relationship between the cumulative signal amplitude and shale pore volume ($R^2 = 0.999$). Thus, the T_2 relaxation spectrum could accurately reflect the shale

water content. The linear correlation between the calibrated cumulative signal amplitude and the pore volume is illustrated in Fig. 2, as depicted by:

$$y = 0.000196x \tag{1}$$

where y represents the pore volume, cm^3; x represents the cumulative signal amplitude; and the R^2 value indicates the correlation between the two variables.

The experiments were carried out under atmospheric pressure (0.1 MPa) and room temperature (26 °C). The experimental setup and procedure are shown in Fig. 3, which included the following steps:

1) The samples were dried at 105 °C for 48 hours in an oven and then transferred to a vacuum desiccator to cool and prevent moisture absorption. After reaching room temperature, the samples were weighed and tested for the total T_2 spectrum, T_1-T_2 spectrum, and layer division T_2 spectrum.
2) Distilled water was added to submerge the bottom of each sample by 5 mm. Initial immersion was marked as the starting point and NMR measurements were taken at specified intervals: 0, 1, 5, 10, 20, 30, 60, 120, 360, 720, 1,440, 2,880, 4,320, 5,760, 7,200, 8,640, and 10,080 minutes. At each designated time point, the sample was removed, the surface was wiped clean, and the NMR measurement was performed. Subsequently, the sample was returned to the water container to continue the spontaneous imbibition experiment.
3) The samples were saturated at 20 MPa for 24 hours and then subjected to NMR measurements.
4) Sequential centrifugation was performed on the samples at speeds of 2,000, 4,000, 6,000, 8,000, 9,000, 10,000, 11,000, and 12,000 rpm for 2 hours each. Table 2 provides the detailed relationships between rotational speed, centrifugal speed and minimum pore radius. NMR measurements were conducted after each centrifugation, resulting in the determination of T_2 cutoff value (T_{2C}). To maintain a consistent core temperature during the centrifugation experiments, the temperature of the centrifuge was set to 25 °C.

2.4 Principle and methodology

2.4.1 Theory of low-field NMR

Based on NMR data, the pore structure and fluid distribution information can be obtained by testing the relaxation characteristics of ^{1}H fluid in porous samples (Hu and Xiao, 2010). Relaxation means a restoring process of the magnetization
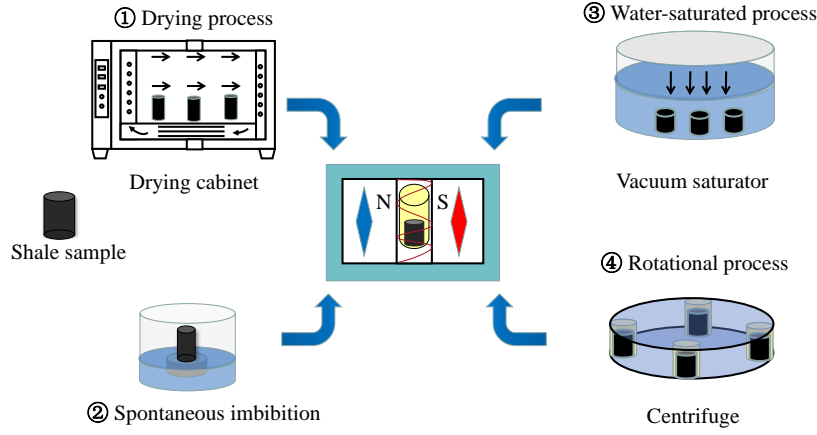
Fig. 3. Diagram of the test equipments and procedures.

vector (M) from non-equilibrium to its equilibrium state. The relaxation times T_1 and T_2 describe the longitudinal and transverse relaxation velocities in the recovery process (Sun et al., 2020).

Liquid protons have similar T_1 and T_2 times, while pseudosolid protons are characterized by a small T_2 time but an elongated T_1 distribution (Fleury et al., 2013). Thus, the longitudinal-transverse relaxation (T_1-T_2) technique was developed to obtain more information on the different proton contributions in shales (Zhang et al., 2020).

T_2 measurements by low-field NMR methods provide valuable insights into pore fluids in porous rocks (Yao et al., 2010). The T_2 distributions are associated with the volume relaxation, surface relaxation and diffusion mechanisms of fluids in porous media. The linear relationship between pore fluid and T_2 can be established from NMR measurements, as shown below:

$$\frac{1}{T_2} = \frac{1}{\rho_2} \frac{S}{V} \tag{2}$$

where ρ_2 represents the surface relaxivity, μm/ms, and S/V represents the ratio of the pore surface area to the pore volume, μm^{-1}.

According to Eq. (2), small pores have shorter T_2 relaxation times than larger pores because they have greater S/V values. As a result, a relationship can be derived that connects T_2 spectra and the pore radius:

$$\frac{S}{V} = \frac{F_s}{r} \tag{3}$$

where F_s represents the pore shape factor, which Eq. (3) for a spherical pore and Eq. (2) for a cylindrical pore, and r denotes the pore radius, μm. Surface relaxivity (ρ_2) is a proportionality constant that characterizes the strength of relaxation induced by the solid and the fluid interface. It is the most significant parameter to connect the relaxation time and the pore radius (Ge et al., 2021), and can also be converted according to Eqs. (2) and (3):

$$r = CT_2 \tag{4}$$

where C represents the product of ρ_2 and F_s.

Table 2. Centrifugal experimental parameters.

Samples	n (rpm)	P_c (MPa)	r (μm)
1	2,000	0.228330	0.637236752
2	4,000	0.913318	0.159309188
3	6,000	2.054966	0.070804084
4	8,000	3.653273	0.039827297
5	9,000	4.623674	0.031468482
6	10,000	5.708240	0.02548947
7	11,000	6.906970	0.021065678
8	12,000	8.219865	0.017701021

2.4.2 Surface relaxivity

Capillary pressure is generated where interfaces between two immiscible fluids exist in the pores (capillaries). This parameter is frequently used to measure the pore throat radius (Marschall et al., 1995). Centrifugal experiments are commonly employed for determining capillary forces. In these experiments, the centrifugal force is primarily assessed through variations in rotational speeds. Assuming that the centrifugal force is equal to the capillary force, the relationship between the centrifugal force and the radius of the pore throat can be obtained by (Thomas et al., 1805; Blunt, 2017):

$$P_c = P_{ci} = \frac{2\sigma\cos\theta}{r} \tag{5}$$

where P_{ci} represents the capillary force, MPa; σ represents the interfacial tension ($\sigma = 72.75 \times 10^{-3}$ N/m); θ is the contact angle ($\theta = 0°$); P_c is the centrifugal force, MPa.

The relationship between centrifugal force and rotational speed is described as (Sing, 1984):

$$P_c = 1.097 \times 10^{-7} \Delta\rho L \left(R_e - \frac{L}{2} \right) n^2 \tag{6}$$

where $\Delta\rho$ represents the density difference between the oil and gas phases, 0.01 g/cm^3; L represents the length of the rock sample ($L = 5$ cm); R_e represents the rotation radius of
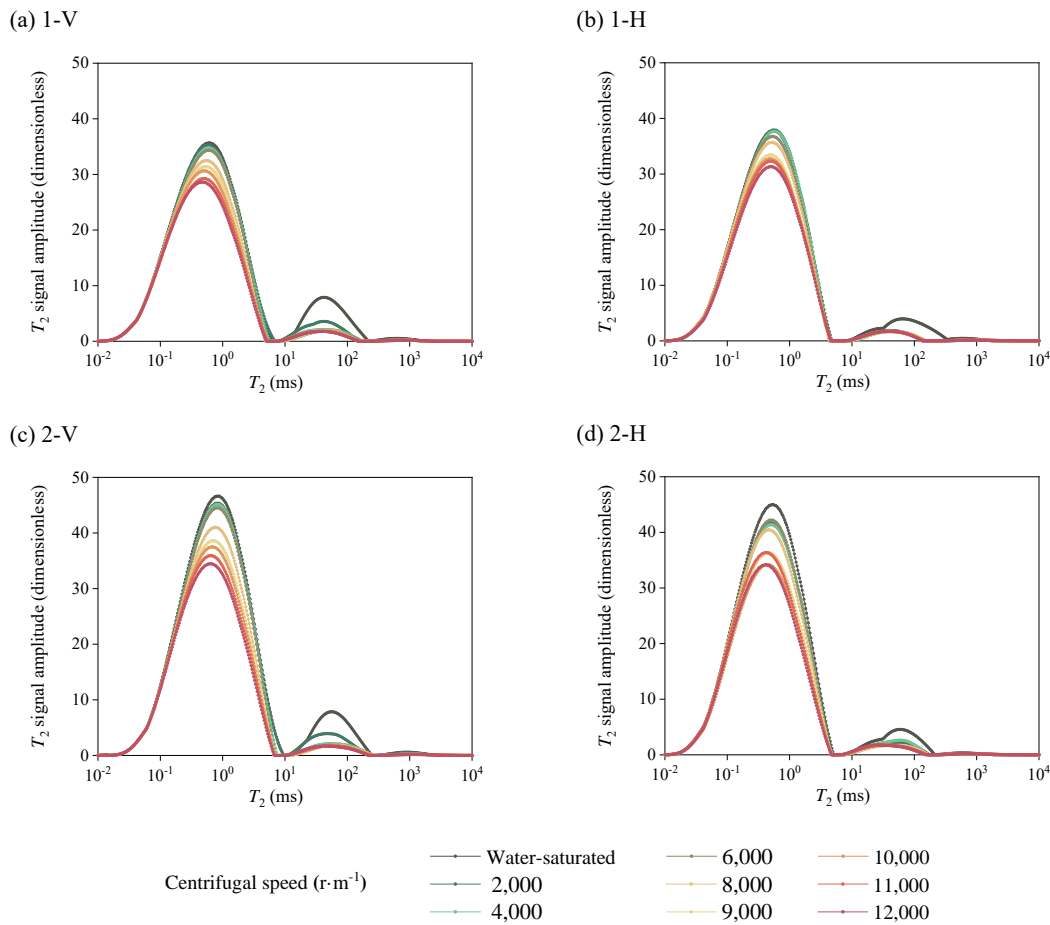
Fig. 4. T_2 distribution of shale samples in the centrifugation process: (a) sample 1-V, (b) sample 1-H, (c) sample 2-V and (d) sample 2-H.

the rock sample in the centrifuge (R_e = 12.9 cm); and n is the centrifugal speed, rpm.

The maximum centrifugal force can be determined by conducting a series of centrifugal experiments, enabling us to obtain the T_2 cutoff values (T_{2C}) for distinguishing mobile water from bound water (Yao et al., 2010). The relationship between T_{2C} and the maximum centrifugal force can then be established to obtain the surface relaxation rate according to Eq. (4). Table 2 presents the detailed relationships among rotational speed, centrifugal pressure and the minimal pore radius for the discharge of water.

3. Results and discussion

3.1 Pore structure characteristics

3.1.1 Maximum centrifugal force

Centrifugation experiments (Fig. 4) allowed us to obtain the T_2 distributions of shale samples at different centrifugation speeds. After the initial centrifugation (2,000 rpm), water in the large pores was expelled. As the centrifugation speed was increased, the T_2 signal amplitude gradually decreased and the center of the left peak shifted to a smaller T_2 value, indicating the migration of fluid from large pores to small pores during

centrifugation. The T_2 signal amplitude attenuated the most when the centrifugation speed was increased from 8,000 to 9,000 rpm. However, there was almost no change when the centrifugation speed was increased from 9,000 to 12,000 rpm, suggesting an optimal centrifugation speed of 9,000 rpm.

During centrifugation, the T_2 signal amplitude of the 1-V and 1-H samples showed little variation, while significant changes were observed in the T_2 signal amplitude of the 2-V and 2-H samples. In particular, the T_2 signal amplitude of large pores in the 2-H sample did not decrease after the initial centrifugation. The shape of peaks in the 1-V and 1-H samples exhibited similar changes to the 2-V and 2-H samples, especially for T_2 relaxation times greater than 10 ms. These results suggested differences in pore structure and fluid distribution among different samples.

3.1.2 Distribution of movable fluid

The state of water in shale pores can be classified into bound and movable (Cai et al., 2013). Bound water is difficult to extract during shale gas production, while movable water is more easily recoverable. T_{2C} serves as a crucial parameter to distinguish between bound water ($T_2 < T_{2C}$) and movable water ($T_2 > T_{2C}$) (Yao et al., 2010). It also reflects the bound-
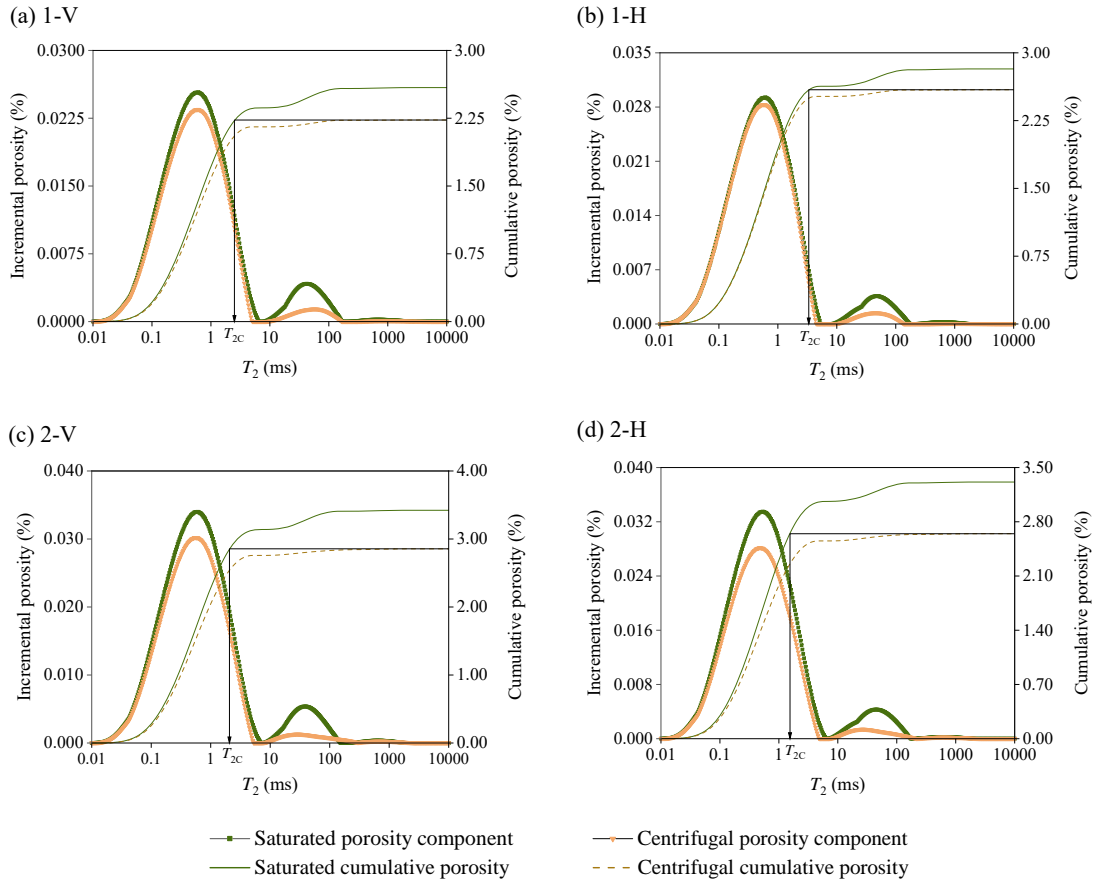
Fig. 5. T_2 cutoff distributions of the shale samples: (a) sample 1-V, (b) sample 1-H, (c) sample 2-V and (d) sample 2-H.
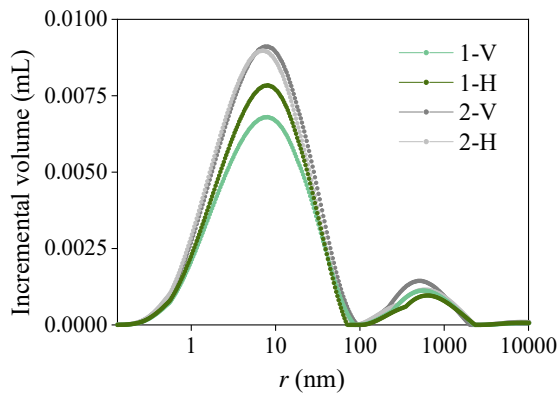

Fig. 6. T_2 distribution of water-saturated shale samples.

ary of fluid flow in pores. When it is higher than this value, the fluid is movable; otherwise, it is bound fluid. The relaxation time of bound water is $T_2 < T_{2C}$ and that of movable water is $T_2 > T_{2C}$. T_{2C} is often obtained by the cumulative integral curve of the T_2 spectrum after high-speed centrifugation (Liu et al., 2018).

In order to determine T_{2C}, the T_2 spectra of saturated and bound water conditions were compared using a standard centrifugation speed of 9,000 rpm (Fig. 5). This corresponds to a centrifugal force of 680 psi, equivalent to a pressure of

approximately 4.62 MPa, which effectively removes liquid from pores with > 0.031 μm radius. The incremental T_2 spectra were converted to cumulative T_2 spectra to obtain T_{2C}. The T_{2C} values for the 1-V, 1-H, 2-V, and 2-H samples were 2.50, 3.35, 2.06, and 1.54 ms, respectively. The T_{2C} values for the 2-V and 2-H samples were smaller than those for the 1-V and 1-H samples, indicating a larger discharge of movable water after centrifugation. The percentages of bound water were 85.88%, 91.68%, 83.22%, and 80.07% for the 1-V, 1-H, 2-V, and 2-H samples, respectively, while those of movable water were 14.12%, 8.32%, 16.78%, and 19.93%, respectively. Sample 1 presented a higher percentage of bound water than Sample 2.

3.1.3 Pore size distribution

In Eq. (4), the pore structure of shale is usually simplified by a spherical model, with F_s taking the value of 3. For subsequent discussion, the average value of T_{2C} was set as 2.3625, the corresponding pore radius was 0.3167 μm, and ρ_2 was 4.44, which is in line with the previous experience range (Li et al., 2022b). Therefore, using Eq. (4), the NMR measurement of the whole pore fluid can be converted into a full-scale pore size distribution to study the pore structure of shale.

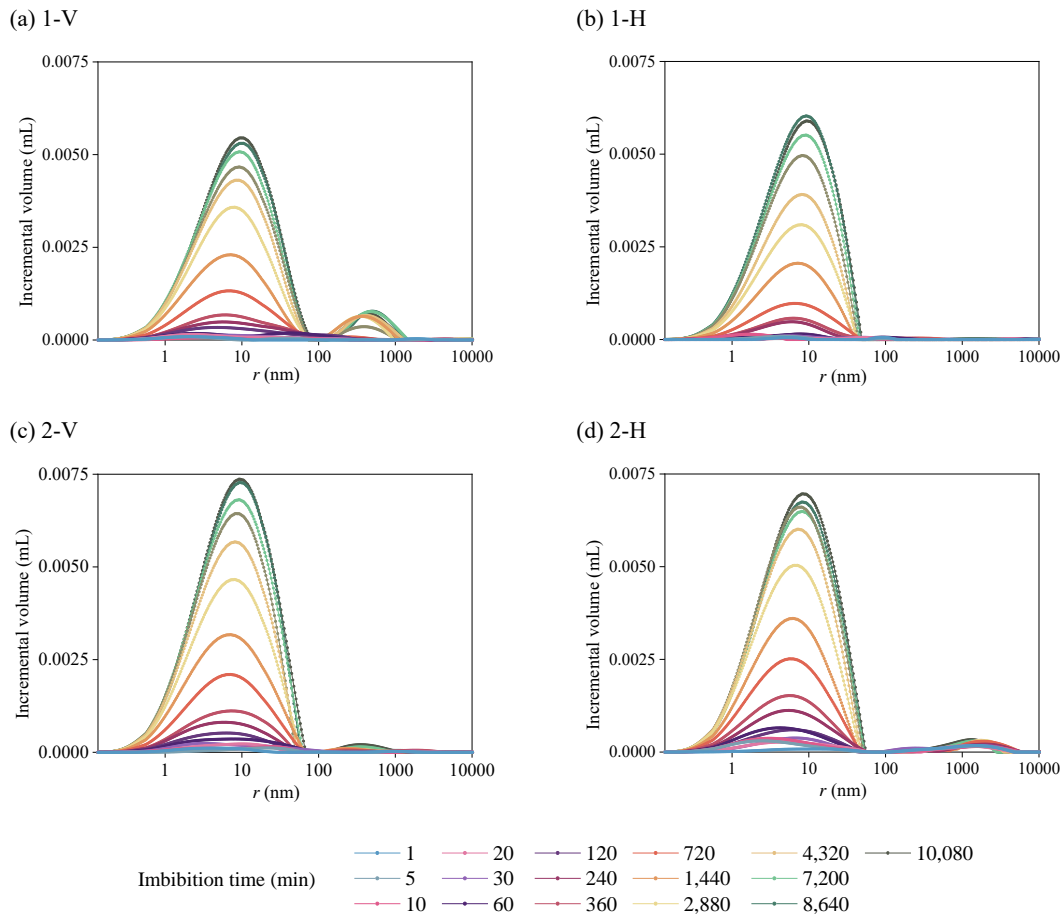The T_2 distribution of water-saturated shale samples re-

Fig. 7. T_2 distribution of shale samples during the spontaneous imbibition experiment: (a) sample 1-V, (b) sample 1-H, (c) sample 2-V and (d) sample 2-H.

vealed bimodal distribution (Fig. 6), with the first peak ranging from 0 to 100 nm and the second peak ranging from 100 to 2,000 nm. The porosity of the samples was mainly attributed to 0 to 100 nm pores, resulting in narrower peaks. Sample 1 exhibited a small pore concentration of approximately 8.3 nm, while Sample 2 had a slightly smaller pore concentration between 7 and 8 nm. The total pore volumes for samples 1-V, 1-H, 2-V, and 2-H were 0.694, 0.757, 0.918, and 0.888 mL, respectively. The corresponding pore volumes for the 0-100 nm range were 0.634, 0.705, 0.842, and 0.821 mL, while the pore volumes for the 100-2,000 nm range were 0.06, 0.052, 0.076, and 0.067 mL, respectively. Notably, the macroporous volume was higher in the 1-V and 2-V samples than in the 1-H and 2-H samples. There was a noticeable gap in pore volume between 0-100 nm for the 1-V and 1-H samples, while this gap was smaller between the 2-V and 2-H samples.

3.2 Spontaneous imbibition characteristics

3.2.1 Imbibition process

A spontaneous imbibition experiment was conducted to observe the variation in imbibition volume among shale samples, excluding the dry substrate data as the baseline. The amplitudes of the T_2 peaks increased at different rates during the experiment. The imbibition curve in Fig. 7 indicated that the maximum imbibition volume occurred on the first day, with the growth rate slowing down after the third day. The imbibition volume reached saturation by days 6 and 7, indicating that the shale sample reached imbibition equilibrium in approximately 7 days.

During the imbibition process, the 0-100 nm pores showed stronger imbibition capacity and experienced a significant volume increase. After 1,440 minutes, the >100 nm pores reached saturation with a minimal volume increase. Further imbibition relied on the 0-100 nm pores. As the imbibition progressed, the pore size contributing to the volume shifted toward the right, indicating an increase in the proportion of 0-100 nm pores.

Sample 1-V exhibited bimodal distribution, while Sample 1-H had unimodal distribution. The peaks corresponding to the 0-100 nm pores demonstrated similar trends among the four samples. Compared to the other samples, 1-V had the largest imbibition volume in the >100 nm pores, while Sample 1-H contributed to the imbibition volume over a wider range of pore sizes, exceeding 1,000 nm.
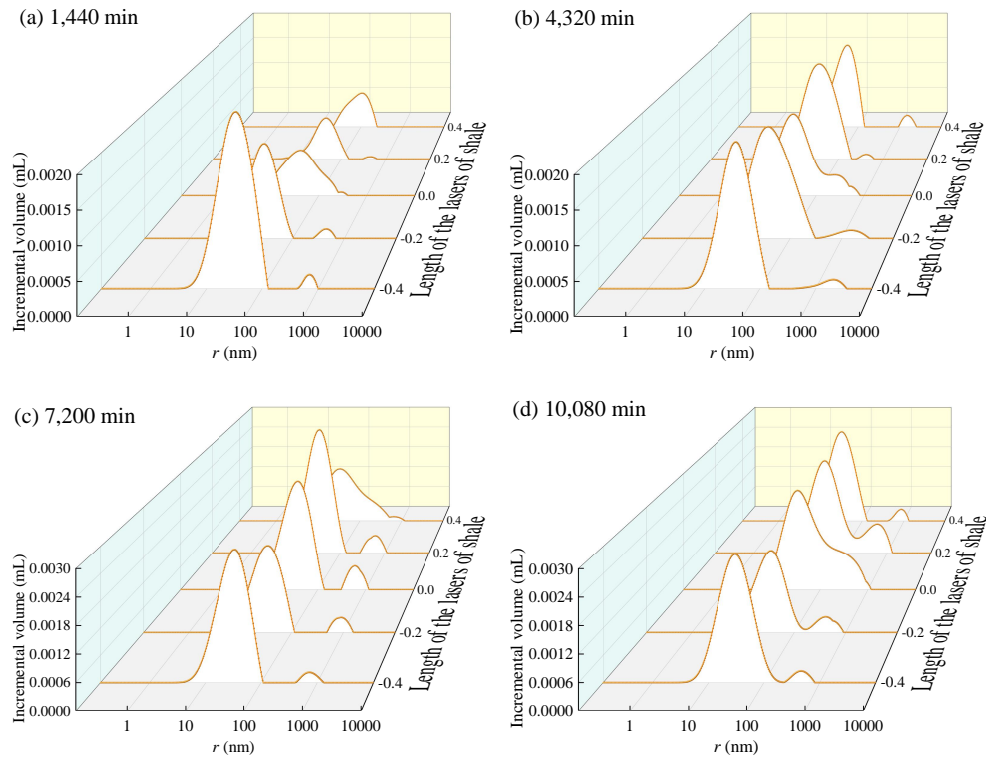
Fig. 8. Layer division T_2 spectrum for the 1-H shale sample during spontaneous imbibition: (a) 1,440 min, (b) 4,320 min, (c) 7,200 min and (d) 10,080 min.
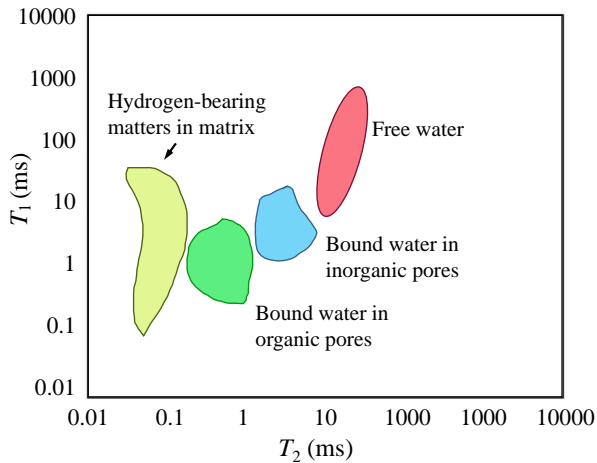

Fig. 9. Pore water division of the T_1-T_2 spectrum (modified from Sun et al. (2020)).

3.2.2 Layer division T_2 and water spatial evolution

Layer division T_2 mapping reveals the upward movement of water at different heights during imbibition. In the 1-H sample (Fig. 8), at 1,440 min, there was a significant increase in water uptake in the 0-100 nm pores in the lower section compared to the upper section, while pores larger than 100 nm only showed uptake in the lower section. At 4,320 min, the discrepancy in uptake between different sections decreased and pores larger than 100 nm started to show uptake in the upper section. At

7,200 min, there was a noticeable increase in uptake for pores larger than 100 nm in all sections. By 10,080 min, improved connectivity was observed for both 0-100 nm pores and pores larger than 100 nm in all sections. In the upper section, pores larger than 100 nm showed almost no uptake at 7,200 min, and the uptake in the 0-100 nm pores was lower than that in the other sections. By 10,080 min, pores larger than 100 nm were near saturation in all sections, and the uptake in the 0-100 nm pores became similar to that in other sections after the stabilization of signal intensity. This is attributed to water entering the upper section through larger pores and diffusing horizontally into smaller pores.

3.2.3 Water distribution

As mentioned in Section 3.1.2, water in shale can be categorized into two types: Free (movable) water and bound water. Free water is found in microcracks and large inorganic pores, while bound water exists in small inorganic pores and partial organic pores (Yan et al., 2017). The presence of different forms of water can be detected through fluid signals, including free water, bound water in inorganic pores, bound water in organic pores, and hydrogen-bearing matter in the matrix. Fig. 9 illustrates the multiphase division of pore water. To investigate these different phases, T_2 and T_1-T_2 spectrum tests were conducted on shale samples at two specific time points: After maximum centrifugal force centrifugation and at imbibition equilibrium.

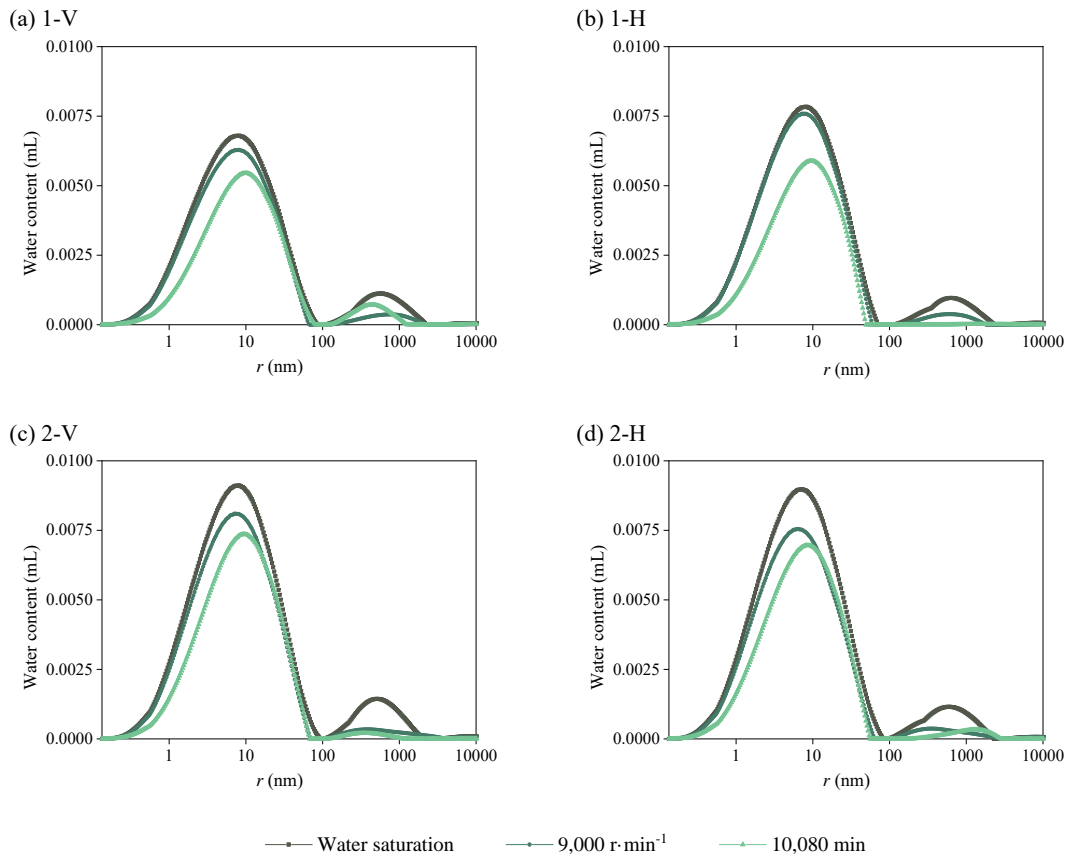After centrifugation, more free water is discharged from

Fig. 10. T_2 distribution of shale samples after full water saturation, maximum centrifugal force centrifugation, and at imbibition equilibrium: (a) sample 1-V, (b) sample 1-H, (c) sample 2-V and (d) sample 2-H.

the large pores because the water in these pores does not easily adhere to the pore surface and is more susceptible to the influence of gravity. Sample 2 had more free water than Sample 1, possibly because of better connectivity in the pore space where the free water resides. Since all pore water after the centrifugation experiment was bound water, the comparison of Fig. 10 shows that the content of pore water at the spontaneous imbibition equilibrium state was lower than that in the centrifugal state, indicating that most pores occupied by bound water contributed to the spontaneous imbibition process, while only a small fraction did not participate in imbibition.

Since the two-dimensional NMR spectrum only represents the proportion of different types of pore water, it was necessary to combine the data from Fig. 10 for analysis. This revealed that in centrifuged samples, due to the higher water content, the proportion of hydrogen-bearing matter in the matrix was lower compared to that in equilibrium imbibition samples. Bound water in both organic and inorganic pores exhibited high proportions, especially bound water in organic pores, indicating a significant contribution of organic matter to the increase in bound water content. From Fig. 1, it can be observed that the Qiongzhusi Formation shale is a carbonaceous shale with high organic matter content, resulting in a larger proportion of bound water in organic pores, which is consistent

with the study of Chao et al. (2021). However, this conclusion still needs further confirmation through other testing methods.

3.3 Imbibition dynamics analysis

3.3.1 Influence of pore structure on imbibition volume

According to the International Union of Pure and Applied Chemistry pore classification, pores can be categorized into micropores (< 2 nm), mesopores (2-50 nm), and macropores (> 50 nm). Because of the difference in cracks between the samples, to evaluate the contribution of macropores in the imbibition process and facilitate subsequent discussion, the macropores were considered as 50-100 nm.

During imbibition, the shale samples exhibited varying trends in the imbibed volume by different-sized pores (Fig. 12). For the 1-V and 1-H samples, micropores drove imbibition until 120 minutes, after which mesopores became dominant. At 1,440 minutes, macropores in sample 1 also contributed to the water volume, while those in sample 2 had a negligible impact. By 4,320 minutes, micropores and macropores in the 1-V and 1-H samples no longer had a significant contribution; imbibition relied solely on mesopores. In contrast, for the 2-V and 2-H samples, mesopores dominated from as early as one minute with the highest pore water volume. By 2,880 minutes, the micropores and macropores in these samples were essentially saturated. Among all four samples, the capacity for
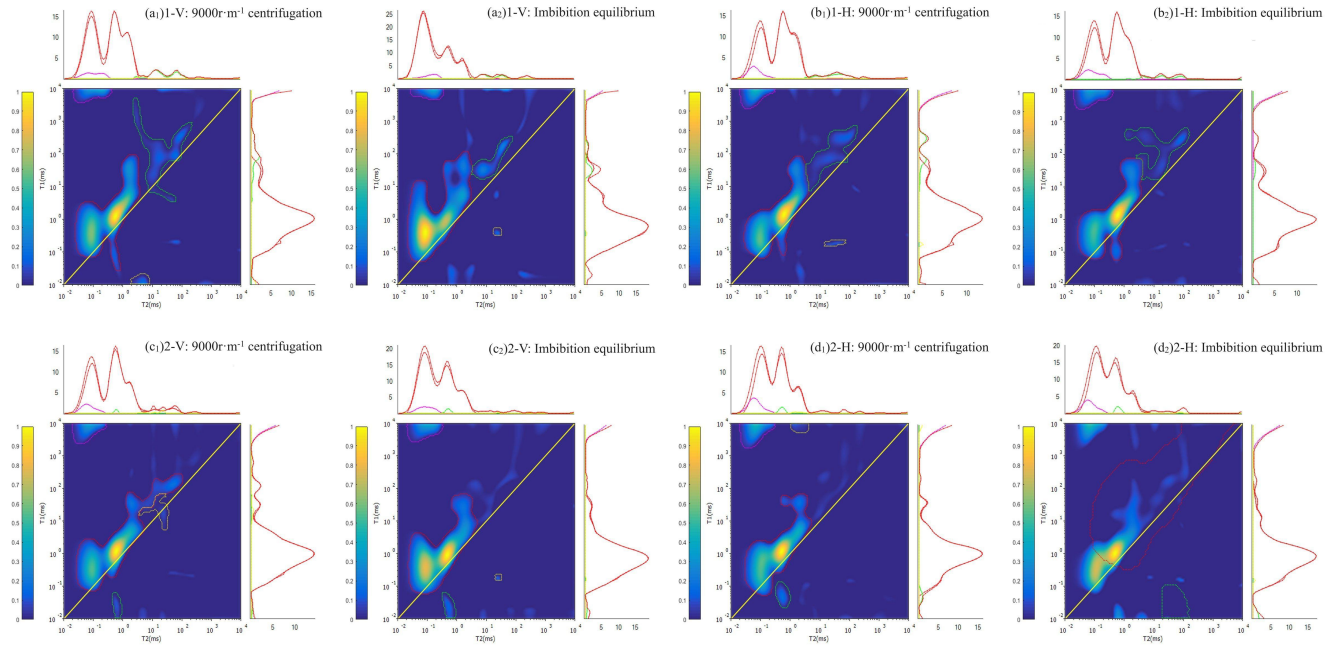
Fig. 11. T_1-T_2 spectra of shale samples after maximum centrifugal force centrifugation and imbibition equilibrium: (a) sample 1-V, (b) sample 1-H, (c) sample 2-V and (d) sample 2-H.
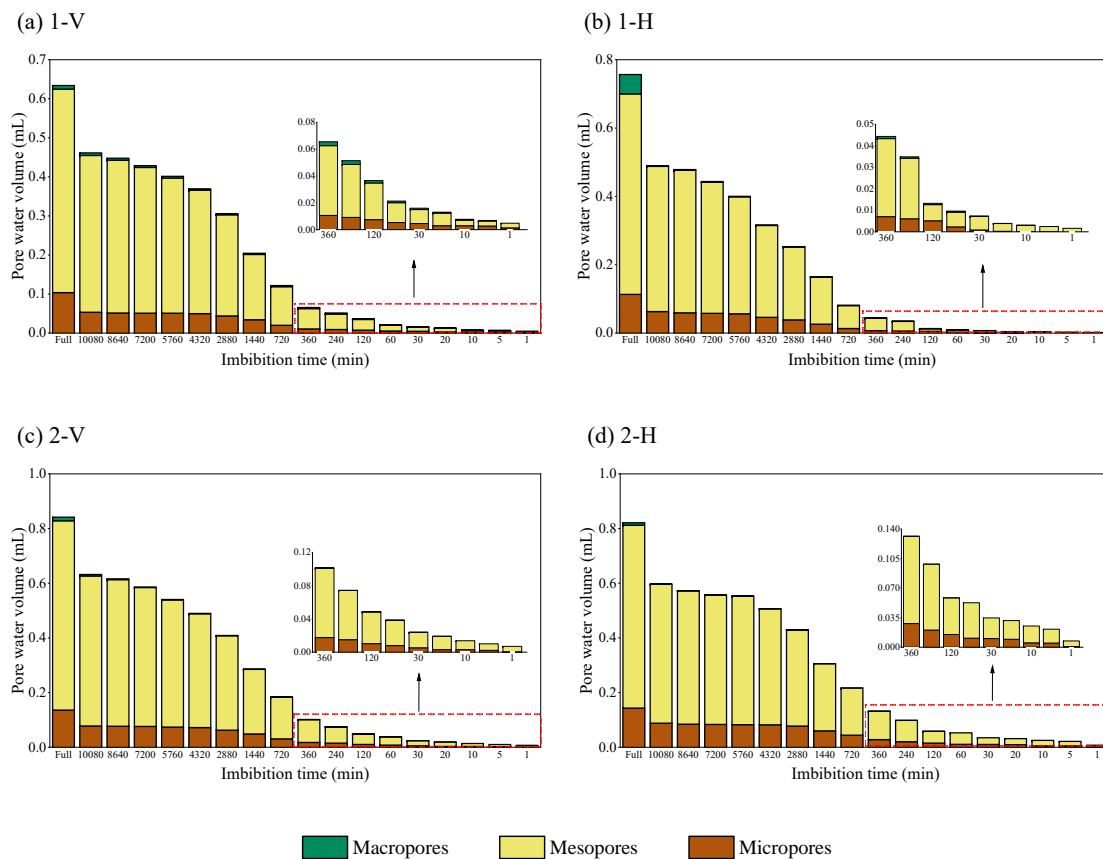

Fig. 12. Contribution of the cumulative imbibition volume of different pore sizes during the imbibition process: (a) sample 1-V, (b) sample 1-H, (c) sample 2-V and (d) sample 2-H.

Fig. 13. Cumulative imbibition volume of different pore sizes during the imbibition process: (a) sample 1-V, (b) sample 1-H, (c) sample 2-V and (d) sample 2-H.
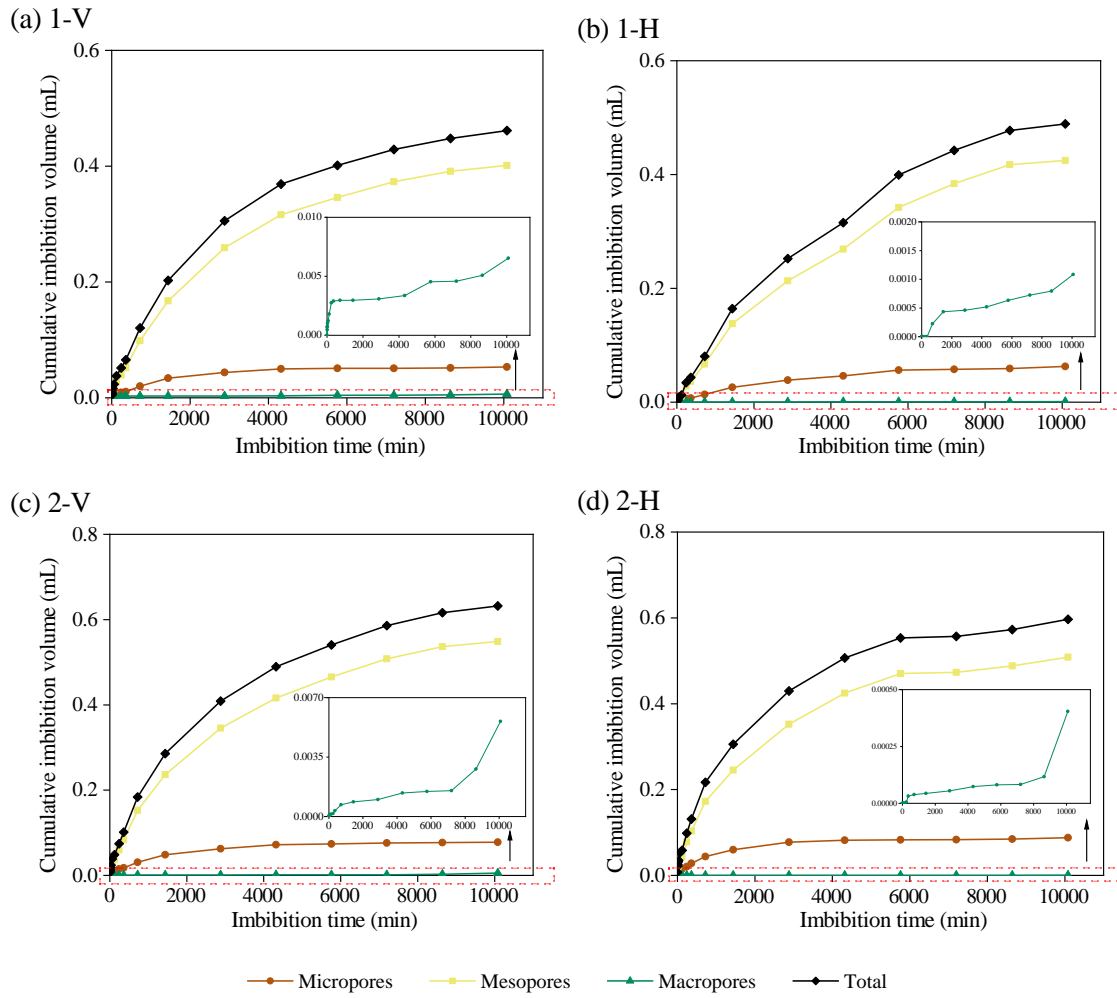
imbibition was stronger in the macropores of the 2-H sample, as it quickly reached saturation during subsequent imbibition.

In comparison to the water-saturated samples, it could be seen that during imbibition equilibrium, micropores in the 1-V, 1-H, 2-V and 2-H samples contributed to the imbibition volume by 51.47%, 55.62%, 57.22%, and 61.42% respectively; this contribution for mesopores was 77.03%, 72.40%, 79.23%, and 75.98%; and 71%, 20.89%, 42.01%, and 4.56% for macropores. During the imbibition process, Sample 2 exhibited a greater contribution from both mesopores and micropores compared to Sample 1. Micropores in horizontal samples showed a higher contribution toward imbibition than vertical samples, whereas the contribution of mesopores was lower in horizontal samples. Half of the macropores in the l-V sample contributed more significantly toward the imbibition volume compared to the l-H sample. Meanwhile, the imbibition contribution from macropores in the 1-V sample was greater than that in the 1-H sample.

As depicted in Fig. 13, the cumulative imbibed volume of mesopores in all four samples exhibits a similar trend to the overall cumulative imbibed volume during the process

of imbibition. The trends in cumulative imbibed volume are comparable for both the 1-V and 1-H samples. The water uptake rates vary depending on pore size, with smaller pores characterized by stronger capillary forces. Therefore, the proportion of mesopores present in shale samples is a crucial factor that determines their water absorption performance, which is reflected by differences in the imbibed water volumes.

3.3.2 Influence of pore structure on imbibition rate

In the spontaneous imbibition experiment, water rises in the sample due to the effective capillary force and imbibition process, which can be simplified as a one-dimensional piston displacement. Handy (1960) makes several assumptions: (1) liquid displaces gas in a piston-like manner, (2) gas pressure is equal at the imbibition front, and (3) imbibition occurs vertically. The experiment fulfills these conditions:

$$V_b^2 = \frac{2P_c \phi k_w A_c^2 S_w}{\mu_w} t \tag{7}$$

where V_b represents the imbibition volume, cm^3; k_w represents the effective liquid permeability, D; A_c represents the contact
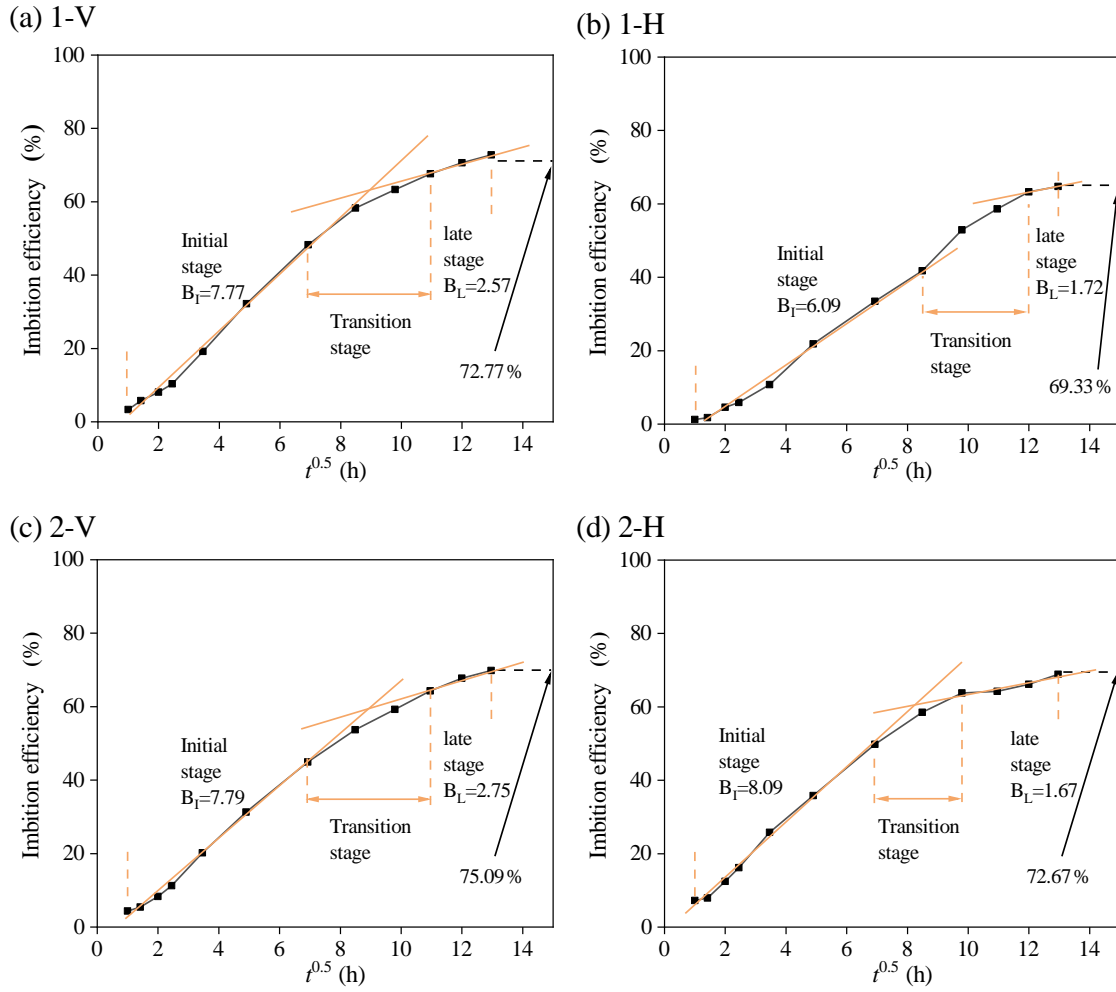
Fig. 14. Classification of imbibition stages: (a) sample 1-V, (b) sample 1-H, (c) sample 2-V and (d) sample 2-H.

area, cm^2; S_w represents the water saturation, %; μ_w represents the viscosity of water, mP; and t is the imbibition time, s. Handy's equation can be converted to:

$$\frac{V_b}{V_s} = \frac{1}{V_s}\sqrt{\frac{2P_c\phi K_w S_w}{\mu_w}}\sqrt{t} \tag{8}$$

where V_s denotes the saturated water volume, cm^3, and V_b/V_s is the normalized imbibition efficiency, %.

Eq. (8) can be simplified to:

$$\frac{V_b}{V_s} = Bt^{0.5} \tag{9}$$

where B represents the imbibition rate. The imbibition curve of shale (Fig. 14) shows three stages: Initial, transition, and later stage. The key parameters characterizing the process are the initial imbibition rate (B_I), late imbibition rate (B_L), and imbibition efficiency. For the 1-V sample, the respective stages are 0-48, 48-120 and 120-168 h; for the 1-H sample, the respective stages are 0-72, 72-144 and 144-168 h. Similarly, the 2-V sample has respective stages of 0-48, 48-120 and 120-168 h, while the 2-H sample has respective stages of 0-48, 48-96 and 96-168 h.

In the initial stage, the B_I values for the samples were as follows: 1-V (7.77), 1-H (6.09), 2-V (7.79), and 2-H (8.09). In the later stage, the B_L values were 1-V (2.57), 1-H (1.73), 2-V (2.75), and 2-H (1.67). The higher B_I value of the 1-V sample in the initial stage is due to its higher imbibition rates compared to the 1-H sample, mainly caused by larger pores (Fig. 15). The B_I value of the 2-H sample is slightly higher than that of the 2-V sample due to the higher imbibition rates of micropores and macropores in this sample, while the mesopore rates are similar between the two. Additionally, the B_L value is higher for vertical samples in the later stage because of the continued increase in the imbibition rate of large pores, while the horizontal samples reach saturation.

At imbibition equilibrium, the imbibition efficiency for the samples is 1-V: 72.77%, 1-H: 69.33%, 2-V: 75.09%, and 2-H: 72.67%, indicating higher efficiency for the vertical samples. The discrepancy between the horizontal and vertical imbibition efficiencies of samples 1-V and 1-H lies in the fact that certain macropores in the vertical sample contribute to its imbibition capacity. On the other hand, differences in imbibition efficiency between samples 1-V and 2-V are independent of macropores and rather stem from variations in material composition and compactness.
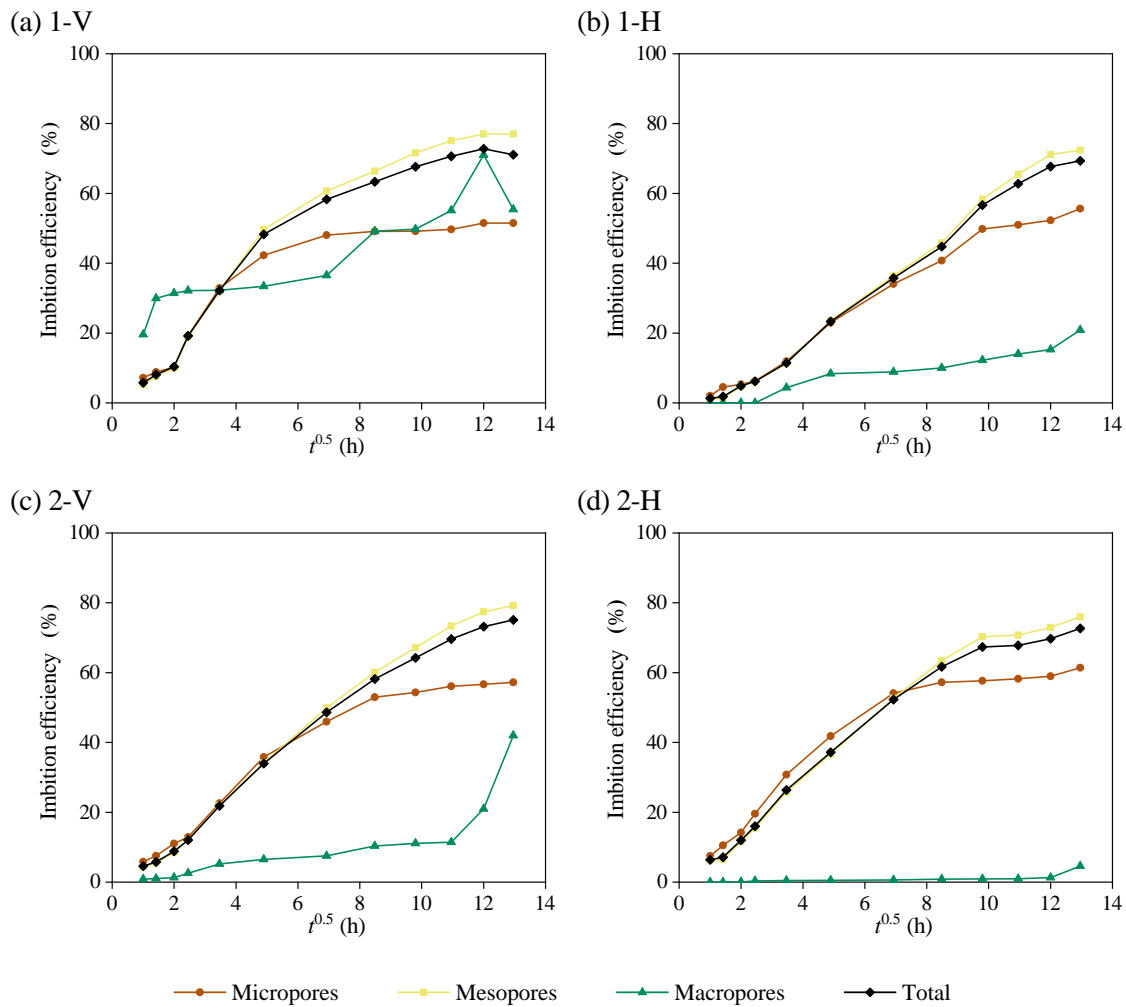
Fig. 15. Water imbibition rate of different pore sizes: (a) sample 1-V, (b) sample 1-H, (c) sample 2-V and (d) sample 2-H.

3.3.3 Variation in imbibition characteristics

1) Different pore network development degrees affect the spontaneous imbibition process.

   From Fig. 15, it is evident that both mesopores and micropores exhibit an initial rapid increase in imbibition efficiency during the imbibition process, followed by gradual saturation. Micropores reach this saturation stage earlier than mesopores. The contribution of mesopores to the imbibition process is relatively significant (Fig. 12); thus, the overall trend of the total imbibition efficiency aligns with that of mesopores. On the other hand, there are slight variations in the behavior of macropores among different samples; however, they generally demonstrate an initial rise followed by a plateau stage and then another rapid ascent. Most samples have limited contributions of macropores to the imbibition process, resulting in a minimal impact on the overall imbibition rate. However, certain samples such as 1-V exhibit unusually high volumes of macropore imbibition, leading to higher initial rates and efficiencies compared to other samples.

2) The bedding development of marine carbonaceous shale

in the Qiongzhusi Formation influences the imbibition process. In this study, vertical samples exhibited higher imbibition rates in the later stages, contradicting the findings of Wang et al. (2021). This discrepancy may be attributed to the well-developed bedding planes in carbonaceous shale. Sample 1 had more pronounced bedding fractures than Sample 2, yielding a significant difference in imbibition efficiency between the horizontal and vertical samples of Sample 1, while Sample 2 showed similar efficiencies. The imbibition rates were similar for the 1-V and 2-V samples, but larger differences were detected between the 1-H and 2-H samples. The interbedding opening and closing scale in the 1-H sample was larger, resulting in a lower imbibition rate.

3) Organic matter and clay minerals play a positive role in the enrichment of the permeable pores of shale. From the two-dimensional NMR tests, it could be observed that bound water in organic pores accounts for a higher proportion during imbibition equilibrium. Sample 2, despite having a similar TOC content as Sample 1, exhibited a higher clay mineral content, larger pore volume (0-100 nm), and greater bound water volume. This resulted in
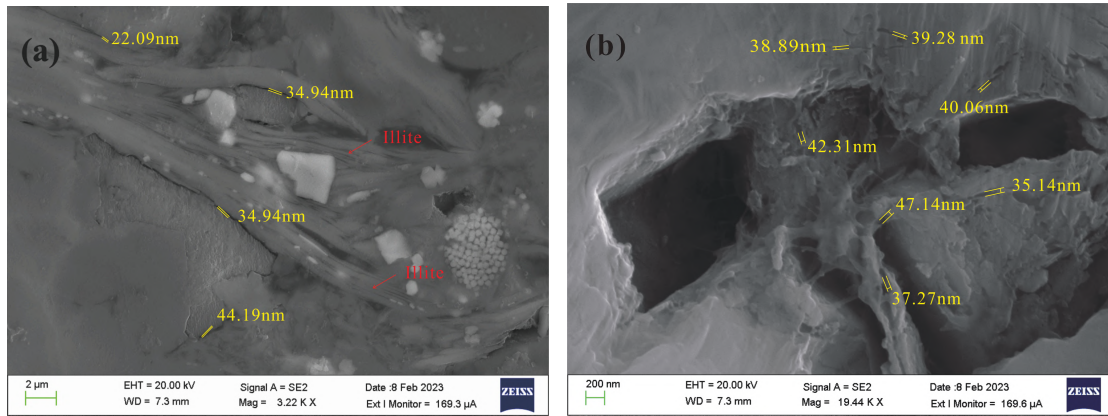
Fig. 16. SEM images of the occurrence of clay minerals and mesopores in shale samples at different magnifications: (a) 3,220 and (b) 19,440.

larger volumes of micropore and mesopore imbibition and greater overall imbibition volume compared to Sample 1. This is because clay minerals extensively develop nanoscale pores, particularly micropores and mesoporous pores (Chen et al., 2016). Fig. 16 shows the occurrence of clay minerals and nanoscale pores in the shale of the Qiongzhusi Formation. The interlayer structure of clay minerals made them develop abundant micropores of approximately 1 nm (Sposito et al., 1999).

4. Conclusions

Focusing on shale samples from the Qiongzhusi Formation, NMR experiments were conducted to investigate spontaneous imbibition in marine shales and the impact of pore structure on imbibition characteristics. The total T_2 spectra, T_1-T_2 spectra, and layer division T_2 spectra were analyzed to understand the involved imbibition mechanisms. The following conclusions were obtained:

1) Mesopores have the greatest impact on the imbibition rate of marine carbonaceous shale, followed by micropores and macropores. The imbibition efficiency shows a rapid initial surge, followed by a gradual leveling off trend. However, macropores reach equilibrium first, followed by micropores and then mesopores. Only macropores show another rapid increase in imbibition toward the end.
2) Due to the bedding characteristics of marine carbonaceous shale, horizontal bedding samples exhibit lower imbibition efficiency than vertical samples. The bedding spacing influences both the macropore imbibition volume and the overall imbibition efficiency.
3) The bound water content after saturation centrifugation exceeds the capillary water absorption capacity of the dry sample at spontaneous imbibition equilibrium, indicating that a significant portion of the pores that provides space for bound water contributes to the spontaneous imbibition ability.
4) In marine carbonaceous shale, the bound water content in organic pores is relatively high during imbibition equilibrium. The presence of clay minerals in shale samples

directly correlates with enhanced imbibition capacity, resulting in increased volumes of micropores and mesopores during the imbibition process.

Nomenclature

y = Pore volume (cm^3)
x = Cumulative signal amplitude
R^2 = Correlation between x and y
P_c = Centrifugal force (MPa)
$\Delta\rho$ = Density difference between oil and gas phases (g/cm^3)
L = Length of rock sample (cm)
R_e = Rotation radius of rock sample (cm)
n = Centrifugal speed (rpm)
σ = Interfacial tension (N/m)
θ = Contact angle (°)
r = Corresponding pore-throat radius (μm)
ρ^2 = Surface relaxivity (μm/ms)
S/V = Ratio of pore surface area to pore volume (μm^{-1})
F_s = Pore shape factor
V_b = Imbibition volume (cm^3)
ϕ = Porosity (%)
k_w = Effective liquid permeability (D)
A_c = Contact area (cm2)
S_w = Water saturation (%)
μ_w = Viscosity of water (mP)
t = Imbibition time (s)
V_s = Saturated water volume (cm^3)
V_b/V_s = Normalized imbibition efficiency (%)
B = Imbibition rate

Acknowledgements

Conflict of interest

The authors declare no competing interest.

References

Barati, R., Liang, J. A review of fracturing fluid systems used for hydraulic fracturing of oil and gas wells. Journal of Applied Polymer Science, 2014, 131(16): 318-323.

Blunt, M. J. Multiphase Flow in Permeable Media: A Pore-Scale Perspective. Cambridge, UK, Cambridge University Press, 2017.

Cai, J. Some key issues and thoughts on spontaneous imbibition in porous media. Chinese Journal of Computational Physics, 2021, 38(5): 505-512. (in Chinese)

Cai, J., Li, C., Song, K., et al. The influence of salinity and mineral components on spontaneous imbibition in tight sandstone. Fuel, 2020, 269: 117087.

Cai, J., Perfect, E., Cheng, L., et al. Generalized modeling of spontaneous imbibition based on Hagen-Poiseuille flow in tortuous capillaries with variably shaped apertures. Langmuir, 2014, 30(18): 5142-5151.

Cai, J., Yu, B. Advances in studies of spontaneous imbibition in porous media. Advances in Mechanics, 2012, 42(6): 735-754. (in Chinese)

Cai, Y., Liu, D., Pan, Z., et al. Petrophysical characterization of chinese coal cores with heat treatment by nuclear magnetic resonance. Fuel, 2013, 108: 292-302.

Chao, Q., Li, S., Shen, W., et al. Study on the spontaneous imbibition characteristics of the deep Longmaxi formation shales of the southern Sichuan basin, China. Geofluids, 2021, 2021: 3563095.

Chen, S., Han, Y., Fu, C., et al. Micro and nanosize pores of clay minerals in shale reservoirs: Implication for the accumulation of shale gas. Sedimentary Geology, 2016, 342: 180-190.

Dou, L., Xiao, Y., Gao, H., et al. The study of enhanced displacement efficiency in tight sandstone from the combination of spontaneous and dynamic imbibition. Journal of Petroleum Science and Engineering, 2021, 199: 108327.

Engelder, T. Capillary tension and imbition sequester frack fluid in Marcellus gas shale. Proceedings of the National Academy of Sciences of the United States of America, 2012, 109(52): E3625.

Fleury, E., Kohler, E., Norrant, S., et al. Characterization and quantification of water in smectites with low-field NMR. The Journal of Physical Chemistry C, 2013, 117(9): 4551-4560.

Flewelling, S, A., Sharma, M. Constraints on upward migration of hydraulic fracturing fluid and brine. Ground Water, 2014, 52(1): 9-19.

Gao, H., Zhu, G., Wang, C., et al. Effects of pore structure and salinity on the imbibition of shale samples using physical simulation and NMR technique: A case from Chang 7 shale, Ordos basin. Simulation, 2019, 97(2): 167-173.

Gao, Z., Hu, Q. Initial water saturation and imbibition fluid affect spontaneous imbibition into Barnett shale samples. Journal of Natural Gas Science and Engineering, 2016, 34: 541-551.

Ge, X., Myers, M., Liu, J., et al. Determining the transverse surface relaxivity of reservoir rocks: A critical review and perspective. Marine and Petroleum Geology, 2021, 126: 104934.

Handy, L. Determination of effective capillary pressures for porous media from imbibition data. Transactions of the AIME, 1960, 219(1): 75-80.

Holditch, S., A. Factors affecting water blocking and gas flow from hydraulically fractured gas wells. Journal of Petroleum Technology, 1978, 31(12): 1515-1524.

Hu, H., Xiao, L. Investigation characteristics of NMR wireline logging tools. Chinese Journal of Magnetic Resonance, 2010, 27(4): 572-583. (in Chinese)

Li, G., Wang, W., Sun, Q., et al. Mathematical model and application of spontaneous and forced imbibition in shale porous media-considered forced pressure and osmosis. Energy & Fuels, 2022a, 36(11): 5723-5736.

Li, X., Chen, S., Wang, Y., et al. Influence of pore structure particularity and pore water on the occurrence of deep shale gas: Wufeng-Longmaxi formation, Luzhou block, Sichuan basin. Natural Resources Research, 2022b, 31(3): 1403-1423.

Li, Y., Yang, J., Pan, Z., et al. Unconventional natural gas accumulations in stacked deposits: A discussion of upper paleozoic coal-bearing strata in the east margin of the Ordos basin, China. Acta Geologica Sinica, 2019, 93(1): 111-129.

Liu, Y., Yao, Y., Liu, D., et al. Shale pore size classification: An NMR fluid typing method. Marine and Petroleum Geology, 2018, 96: 591-601.

Lu, Y., Liu, D., Cai, Y., et al. Spontaneous imbibition in coal with in situ dynamic micro-CT imaging. Journal of Petroleum Science and Engineering, 2022, 208: 109296.

Ma, Y., Yan, M., Zhang, X., et al. NMR experiments on the migration characteristics of water in bedding-bearing low rank coal. Petroleum Science and Technology, 2023: 1-22.

Marschall, D., Gardner, J. S., Mardon, D., et al. Method for correlating NMR relaxometry and mercury injection data. Paper SCA 9511 Presented at International Symposium of the Society of Core Analysts, San Francisco, California, USA, September, 1995.

Meng, M., Ge, H., Shen, Y., et al. The effect of clay-swelling induced cracks on imbibition behavior of marine shale reservoirs. Journal of Natural Gas Science and Engineering, 2020, 83: 103525.

Middleton, R. S., Carey, J. W., Currier, R. P., et al. Shale gas and nonaqueous fracturing fluids: Opportunities and challenges for supercritical CO_2. Applied Energy, 2015, 147: 500-509.

Roychaudhuri, B., Tsotsis, T., Jessen, K. An experimental investigation of spontaneous imbibition in gas shales. Journal of Petroleum Science and Engineering, 2013, 111: 87-97.

Shen, Y., Ge, H., Meng, M., et al. Effect of water imbibition on shale permeability and its influence on gas production. Energy & Fuels, 2017, 31(5): 4973-4980.

Sing, K. W. S. Reporting physisorption data for gas/solid systems with special reference to the determination of surface area and porosity. Pure & Applied Chemistry, 1984, 57(4): 603-619.

Sposito, G., Skipper, N., Sutton, R., et al. Surface geochemistry of the clay minerals. Proceedings of the National Academy of Sciences of the United States of America, 1999, 96(7): 3358-3364.

Sun, Y., Li, Q., Chang, C., et al. NMR-based shale core imbibition performance study. Energies, 2022, 15(17): 6319.

Sun, Y., Zhai, C., Xu, J., et al. A method for accurate characterization of the pore structure of a coal mass based on two-dimensional nuclear magnetic resonance T1-T2. Fuel, 2020, 262: 116574.

Thomas, Y. An essay on the cohesion of fluids. Philosophical Transactions of the Royal Society of London, 1805, 95: 65-87.

Wang, X., Wang, M., Li, Y., et al. Shale pore connectivity and influencing factors based on spontaneous imbibition combined with a nuclear magnetic resonance experiment. Marine and Petroleum Geology, 2021, 132: 105239.

Xue, H., Ding, G., Dong, Z., et al. Study on the wettability and spontaneous imbibition characteristics of lacustrine shale. Geofluids, 2022, 2022: 4023435.

Yan, W., Sun, J., Cheng, Z., et al. Petrophysical characterization of tight oil formations using 1D and 2D NMR. Fuel, 2017, 206: 89-98.

Yao, Y., Liu, D. Comparison of low-field NMR and mercury intrusion porosimetry in characterizing pore size distributions of coals. Fuel, 2020, 95: 152-158.

Yao, Y., Liu, D., Yao, C., et al. Petrophysical characterization of coals by low-field nuclear magnetic resonance (NMR). Fuel, 2010, 89(7): 1371-1380.

Yildiz, C., Akin, A. A mechanistic investigation on the formation and rearrangement of silaspiropentane: A theoretical study. Journal of Molecular Modeling, 2016, 22(7): 158.

Yue, J., Wang, Z., Chen, J. Investigation of timing characteristics of the imbibition height of remolded coal without gas. Energy Sources, Part A: Recovery, Utilization, and Environmental Effects, 2019, 41(2): 156-166.

Zhang, P., Lu, S., Li, J., et al. 1D and 2D nuclear magnetic resonance (NMR) relaxation behaviors of protons in clay, kerogen and oil-bearing shale rocks. Marine and Petroleum Geology, 2020, 114: 104210.

Zhao, Y., Sun, Y., Liu, S., et al. Pore structure characterization of coal by NMR cryoporometry. Fuel, 2017, 190: 359-369.

Zhu, J., Chen, J., Duanmu, X., et al. Experimental study on the distribution and height of spontaneous imbibition water of Chang 7 continental shale oil. Fractal and Fractional, 2023, 7(6): 428.

Zhu, Y., Li, Z., Lai, F. Effects of microscopic pore structures on the spontaneous imbibition of Longmaxi shale. Energy & Fuels, 2022, 36(14): 7456-7471.

Zou, C., Dong, D., Wang, Y., et al. Shale gas in China: Characteristics, challenges and prospects (I). Petroleum Exploration and Development, 2015, 42(6): 753-767.

Zou, C., Zhu, R., Chen, Z., et al. Organic-matter-rich shales of China. Earth-Science Reviews, 2019, 189: 51-78.